

Finite element simulation of crystal plasticity in the tensile fracture behavior of selective laser melting CoCrFeNiMn high entropy alloy

*Wei Duan^{1,2}, Liang-liang Wu¹, Wen Li⁴, Xu Shen⁴, *Yan Zhang^{1,3}, Xiao-yuan Ji⁴ and Jian-xin Zhou⁴

- Key Laboratory of Metallurgical Equipment and Control Technology, Ministry of Education, Wuhan University of Science and Technology, Wuhan, 430081, China
 - Hubei Key Laboratory of Mechanical Transmission and Manufacturing Engineering, Wuhan University of Science and Technology, Wuhan, 430081, China
 - 3. Precision Manufacturing Institute, Wuhan University of Science and Technology, Wuhan, 430081, China
- State Key Laboratory of Materials Processing and Die and Mould Technology, Huazhong University of Science and Technology, Wuhan, 430074, China

*Corresponding address: No. 947, Heping Avenue, Qingshan District, Wuhan City, Hubei Province, China e-mail: duanwei@wust.edu.cn, yanzh@wust.edu.cn

Abstract: The CoCrFeNiMn high-entropy alloy (HEA) exhibits significant potential for engineering applications owing to its exceptional mechanical properties, including high strength, excellent corrosion resistance, and remarkable ductility. HEA fabricated via selective laser melting (SLM) demonstrate significantly enhanced comprehensive performance compared to those produced by casting or other conventional forming methods. Furthermore, the SLM technique enables the direct fabrication of complex structural components. These advantages indicate that SLM HEA possess substantial research potential. This study employs a crystal plasticity theoretical model to investigate grain boundary fracture mechanisms in SLM CoCrFeNiMn HEA columnar crystal model under tensile loading. The proposed model incorporates Cohesive elements with damage evolution criteria within polycrystalline representative volume elements (RVE) to simulate intergranular fracture processes. The simulation results exhibit substantial agreement with the experimentally obtained stress-strain curves, demonstrating that the crystal plasticity constitutive model combined with the cohesive constitutive model can effectively characterize both the macroscopic mechanical response and fracture failure mechanisms of the CoCrFeNiMn HEA. The research finds that the anisotropy coefficients for yield strength, tensile strength, and elongation in the CoCrFeNiMn HEA were determined to be 3.3%, 5.7%, and 22.4%; The polycrystalline elongation increased from 7.7% to 16.7%, while the anisotropy coefficients of yield strength, tensile strength, and elongation decreased by 7.6%, 3.3%, and 27%, following the equiaxialization of columnar grains; Variations in texture strength can significantly influence crack initiation and propagation in CoCrFeNiMn HEA.

Keywords: CoCrFeNiMn high-entropy alloy; crystal plasticity finite element method; Cohesive element; fracture behavior

1 Introduction

The concept of high-entropy alloys (HEAs) was first proposed by Yeh J.^[1], a scholar from Tsinghua University, in 2004. The CoCrFeNiMn HEA is widely utilized in aerospace applications, corrosion-resistant coatings, and mold manufacturing due to its excellent thermal stability, superior corrosion resistance, and high fatigue resistance^[2-4]. The CoCrFeNiMn HEA, characterized by its simple and stable single-phase face-centered cubic (FCC) structure, has garnered significant attention among

researchers^[5]. Laplanche et al.^[6] conducted tensile experiments on the as-cast CoCrFeNiMn HEA at room temperature (293 K) to obtain its stress-strain curve. The results demonstrated that the yield strength and tensile strength of the alloy were 265 MPa and 600 MPa. The ascast CoCrFeNiMn HEA often exhibit issues such as compositional segregation, pore defects, and inclusions. Among these, compositional segregation can significantly deteriorate the mechanical properties of HEA^[7]. Brif Y et al.^[8] reported the first use of laser selective melting (SLM)

to fabricate HEA. The FeCoCrNi HEA produced via SLM exhibited no signs of segregation. Compared to as-cast FeCoCrNi HEA, the SLM-fabricated counterparts demonstrated significantly enhanced properties. Specifically, the yield strength of the SLM HEA reached 600 MPa, which was more than three times higher than the 188 MPa yield strength of the cast alloys.

Gu et al.^[9] conducted an investigation into the anisotropy of the microstructure and mechanical properties of FeCoNiCr0.5 HEA fabricated via SLM. The findings revealed that the scanning direction was characterized by equiaxed grains with grain sizes ranging from 40 to 60 µm, while the building direction was characterized by columnar grains with lengths spanning from 80 to 100 µm. This microstructural difference resulted in the anisotropic tensile behavior of the specimens. Kim et al.[10] employed SLM to fabricate CoCrFeMnNi HEA specimens, achieving yield strengths of 778.4 MPa and 703.5 MPa along the scanning direction and building direction. To mitigate anisotropy, researchers[11, 12] have employed various post-processing techniques aimed at eliminating columnar grains along the deposition direction. Ng et al.[11] demonstrated that hot isostatic pressing (HIP) facilitated the transformation of the Ti-3Al-8V-6Cr-4Mo-4Zr alloy from a columnar to an equiaxed grain structure, while also achieving a substantial grain refinement of up to 72.5%. Furthermore, Dolzhenko et al.[13] reported that the texture strength increased significantly with rising temperature, thereby enhancing the mechanical properties of Cu-Ni-P alloys through heat treatment. Currently, the influence of additively manufactured columnar grain structures on mechanical properties and grain boundary fracture mechanisms remains unclear, while experimental verification entails high costs. This study employs numerical simulations to investigate the effects of columnar grain morphology (with varying aspect ratios) and texture strength on mechanical properties and fracture behavior.

With the ongoing advancement of numerical simulation techniques, an increasing number of researchers^[14-16] have investigated the mechanical behavior of materials by developing material constitutive models and integrating them with numerical simulations. Based on the theory of crystal plasticity, Dang et al.^[17] have established a two-dimensional lamellar organization representative volume element (RVE) model. The model predicted the crack initiation location and propagation path of TC4 alloy under tensile load by adjusting the ratio and distribution of the duplex layer microstructure. Shuyu Wang et al.^[16] conducted crystal plasticity finite element (CPFE) simulations to investigate the tensile fracture behavior of CrMnFeCoNi HEA. The results demonstrated

that cracks initially nucleate at stress concentration sites and subsequently propagate along grain boundaries until final fracture. Moreover, crystallographic orientation was found to significantly influence both crack nucleation and propagation. Shuyu Wang et al. employed the crystal plasticity constitutive model and the Cohesive constitutive model. These models are capable of accurately simulating the continuous variation of stress at grain boundaries, the occurrence of damage, and the initiation and propagation of cracks until the fracture of HEA under loading. Nevertheless, Shuyu Wang et al. did not conduct research on the tensile fracture of the columnar crystal model. As a result, they were unable to offer a viable crystal plasticity simulation study for the tensile fracture of SLM CrMnFeCoNi HEA.

The crystal plasticity finite element method (CPFEM) integrates the theory of crystal plasticity with the finite element method to characterize the evolution of the material microstructure and the macroscopic deformation behavior. In this study, a polycrystalline finite element model of SLM CoCrFeNiMn HEA is established using NEPER software. Stress changes, damage evolution, and crack propagation at grain boundaries are simulated using cohesive elements, while the finite element implementation is performed via the userdefined material subroutine (UMAT) in ABAQUS software. This approach enables a systematic investigation of the roomtemperature tensile fracture behavior of the SLM CoCrFeNiMn HEA, while the model's accuracy is validated by fitting with Wang Fuchao's[18] tensile fracture stress-strain test curve. This research further elucidates the influence of different columnar crystal morphologies on the mechanical properties and anisotropy of the CoCrFeNiMn HEA, as well as the influences of texture strength in crack initiation and propagation.

2 Modeling

2.1 Crystal plastic constitutive model

The crystal deformation comprises both elastic deformation arising from lattice distortion and plastic deformation resulting from dislocation slip, twinning, and phase transition. The total deformation gradient can be expressed as follows:

$$F = F^e F^p \tag{1}$$

where the total strain gradient is denoted by F, F^e represents the elastic deformation, and F^p represents the plastic strain. The rate of the plastic deformation gradient is further related as follows:

$$L^{p} = R^{p} (F^{p})^{-1} = \sum_{\alpha=1}^{N} R^{p} s^{\alpha} \otimes m^{\alpha}$$
 (2)

where \mathcal{K}^{α} is the shear strain rate on the α th slip system,

 s^{α} is the slip direction of the α -slip system, m^{α} is the direction of the slip plane of the α -slip system, and N is the total number of slip systems.

The shear strain rate \mathcal{M} generated by the dislocation motion of each slip coefficient obeys an exponential relationship with the slip shear force:

$$\mathcal{H}^{\alpha} = \mathcal{H}^{\alpha} \left(\frac{\tau^{\alpha}}{g^{\alpha}} \right) \left| \frac{\tau^{\alpha}}{g^{\alpha}} \right|^{n-1} \tag{3}$$

where τ^{α} is the resolved shear stress, g^{α} denotes the slip resistance, and n represents the shear strain sensitivity coefficient. The slip resistance g^{α} is associated with dislocations and can be expressed as:

$$g^{\alpha} = h_{\alpha\beta} g^{\alpha\beta} \tag{4}$$

where $\&^{\alpha}$ is the rate of change of slip resistance and $h_{\alpha\beta}$ is the hardening modulus between slip systems, when $\alpha = \beta$, it indicates self-hardening modulus; when $\alpha \neq \beta$, it indicates latent hardening modulus, and PIERCE^[19] proposed the specific hardening modulus to be expressed as follows:

$$h_{aa} = h(\gamma) = h_0 \operatorname{sech}^2 \left| \frac{h_0 \gamma}{\tau_s - \tau_0} \right|$$
 (5)

$$\gamma = \sum_{\alpha=1}^{N} \int_{0}^{t} |\mathfrak{R}^{\alpha}| \, \mathrm{d}t \tag{6}$$

$$h_{\alpha\beta} = qh(\gamma)(\alpha \neq \beta) \tag{7}$$

where h_0 is the initial hardening modulus, γ is the cumulative shear strain over all slips, τ_0 is the initial critical shear stress, τ_s denotes the saturated rheological stress, and q denotes the hardening parameter ratio, which is taken to be 1.0~1.4 by default.

2.2 Cohesive constitutive model

The cohesive model can effectively capture energy dissipation state evolution and stress during polycrystalline fracture. Additionally, it can be employed to represent grain boundaries between crystals, enabling the simulation of fracture processes in real polycrystalline materials. The cohesive constitutive model is defined a bilinear through traction-detachment response criterion^[20] to define it. The model can be divided into two distinct phases (Figure.1). The first phase corresponds to the linear elastic behavior of the cohesive element, where the curve slope is determined by the cohesive stiffness prior to material damage initiation. The second phase represents the linear softening behavior of the cohesive element following damage initiation, where the traction force reaches its peak value and the cohesive element begins to degrade.

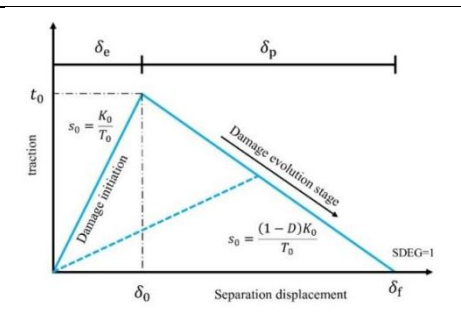


Figure.1 Bilinear traction-separation response of cohesive element

The following relationship is satisfied between the separated displacements and strains of the Cohesive elements:

$$\begin{cases}
\delta^{n} \\
\delta^{s} \\
\delta^{t}
\end{cases} = T_{0} \begin{cases}
\varepsilon^{n} \\
\varepsilon^{s} \\
\varepsilon^{t}
\end{cases}$$
(8)

where δ^n , δ^s , δ^t are the nodal displacements in the normal and orthogonal shear directions of the Cohesive unit, respectively; ε^n , ε^s , ε^t are the strains in the normal and orthogonal shear directions of the Cohesive unit, respectively; and T_0 is the initial thickness of the Cohesive unit, which is generally taken to be 1.

Neglecting the coupling between tensile and shear deformation, the relationship between the traction force (t) applied to the Cohesive element and its nominal strain (ε) can be described by an elastic stiffness matrix as follows:

$$\mathbf{t} = \begin{pmatrix} t_n \\ t_s \\ t_t \end{pmatrix} = \begin{bmatrix} K_0^{nn} & 0 & 0 \\ 0 & K_0^{ss} & 0 \\ 0 & 0 & K_0^{tt} \end{bmatrix} \begin{pmatrix} \boldsymbol{\varepsilon}_n \\ \boldsymbol{\varepsilon}_s \\ \boldsymbol{\varepsilon}_t \end{pmatrix} = \mathbf{K}\boldsymbol{\varepsilon}$$
(9)

Figure 1 illustrates that the inflection point of the bilinear traction-separation response curve corresponds to the initial damage point of the Cohesive element. In this study, the maximum strain damage criterion is employed to determine the initiation of damage in the Cohesive element. The relationship can be expressed as follows:

$$max\left\{\frac{\langle \mathcal{E}_n \rangle}{\mathcal{E}_n^0}, \frac{\mathcal{E}_s}{\mathcal{E}_s^0}, \frac{\mathcal{E}_t}{\mathcal{E}_t^0}\right\} = 1 \tag{10}$$

where '<>' is the Macaulay bracket and ε_n^0 , ε_s^0 , ε_t^0 are the critical strains for damage initiation under pure tension and shear loading, respectively. Once the maximum strain damage criterion is satisfied, the Cohesive element initiates damage evolution. During this process, the traction force gradually diminishes as the relative displacement of the Cohesive element increases. Upon complete degradation (i.e., when the traction force reaches zero), the Cohesive element is eliminated from the simulation, corresponding microscopically to grain

boundary fracture. The damage evolution of the Cohesive element can be characterized by the following equation:

$$t = (1 - D)\overline{t}K = (1 - D)K_0 \tag{11}$$

Where \overline{t} represents the traction force of the cohesive unit prior to damage consideration, K_0 denotes the initial stiffness of the material, and D is the damage evolution variable, which ranges from 0 to 1. The expression for D is given as follows:

$$D = \begin{cases} 0 & \delta < \delta_0 \\ \frac{\delta_{\rm f}(\delta - \delta_0)}{\delta(\delta_{\rm f} - \delta_0)} & \delta \overline{H} \delta_0 \end{cases}$$
 (12)

where δ_0 is the separation displacement at the initial damage of the Cohesive unit; $\delta_{\rm f}$ is the nodal displacement at the final fracture of the Cohesive element.

2.3 HEA finite element model

Li et al.^[21] prepared three CoCrFeNiMn HEA samples via SLM. By adjusting SLM process parameters, including laser power, scanning speed, and layer thickness, they obtained samples with an average grain size of approximately 22 μm. In this study, a representative volume element (RVE) containing 80 Voronoi grains was generated using NEPER software^[22], with dimensions of 1 mm × 1 mm × 1 mm based on the average grain size. The columnar crystals were assigned an average aspect ratio of (1, 0.4, 0.4). Cohesive elements were employed to simulate the grain boundaries of the polycrystalline structure, as illustrated in Fig. 2. The grid cell types of the model grain boundaries and grains are C3D4 cells and COH3D6 cells respectively.

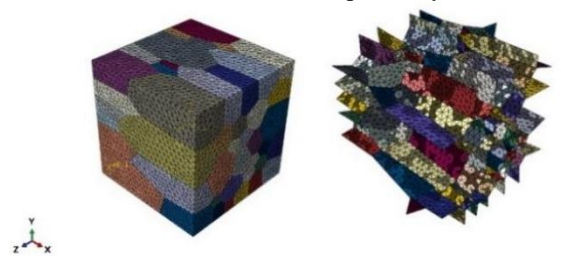


Figure.2 CoCrFeNiMn HEA polycrystalline model grains and grain boundaries

To avoid inaccurate simulation results caused by rigid body displacement of the RVE model under loading during finite element analysis, appropriate constraints must be applied to the model. As shown in Fig. 3, a coordinate system is established in the lower left corner, and the degrees of freedom in the X, Y, and Z directions are set to be U_1 , U_2 , and U_3 , respectively. constraints are added to all nodes in the XOY plane: U_3 =0; to all nodes in the YOZ plane: U_1 =0; and to all nodes in the XOZ plane: U_2 =0; The reference point RP-1 is kinematically coupled to all nodes on its nearest XOY plane, and a tensile displacement load of U_3 = 0.05 mm is applied at

RP-1.

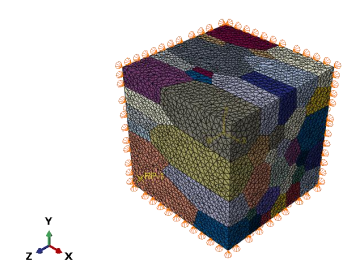


Figure.3 HEA polycrystal model constraints and boundary conditions

2.4 Determination of parameters of HEA

According to the findings reported by Fang et al. [23], the three elastic constants of CoCrFeNiMn HEA polycrystals were determined as C11 = 264.6 GPa, C12 = 184.8 GPa, and C44 = 112.9 GPa. The material parameters required for the UMAT subroutine were obtained through finite element simulation of a CoCrFeNiMn HEA polycrystalline model, combined with stress-strain curve fitting based on tensile fracture experiments conducted by Wang et al. These parameters were automatically assigned to the corresponding elements via custom code. The key material properties include: Elastic constants, Initial hardening modulus, Initial critical shear stress , Saturated yield stress , Cohesive element elastic constants . Initial damage displacement and so on. The material parameters can be determined by the trial and error method in comparison with the experimentally obtained stress-strain curve fits, and the fitted material parameters are shown in Table 1.

Table.1 CoCrFeNiMn HEA material parameters

Parameter	Symbol	Value
Initial hardening modulus(Mpa)	H_0	70.5
Saturated yield stress(Mpa)	$ au_{ m s}$	260.5
Initial critical shear stress(Mpa)	τ_0	130.5
Strain rate sensitivity coefficient	n	10
Reference shear strain rate (s ⁻¹⁾	γο	0.002
Hardening factor	q	1
Failure node displacement(mm)	$\delta_{ m f}$	0.0012

As shown in Figure. 4, the stress-strain curves were obtained from the polycrystalline CoCrFeNiMn HEA model under tensile loading conditions. The green circular curve represents the experimental stress-strain curve from room-temperature tensile tests conducted by

Wang et al.^[18], while the red five-pointed star curve corresponds to the simulated curve. As shown in Figure. 4, the experimental and simulation curves exhibit good agreement, confirming the validity of the constitutive model and material parameters presented in this study. CPFE method effectively bridges the micro-deformation mechanisms and macro-deformation behavior of the material. Furthermore, by incorporating cohesive elements at the grain boundaries in the model, the approach successfully captures the intergranular fracture behavior of the material.

2.5 Polycrystalline modelling of HEA with different grain morphologies

The SLM process characteristics will lead to columnar crystals along the building direction, and grain refinement can effectively improve the mechanical properties of the material. The CoCrFeNiMn HEA polycrystalline model with different columnar crystal morphology is generated by adjusting the average aspect

ratio of the grains, and the average aspect ratios of the polycrystalline finite element model are: (1,0.1,0.1), (1,0.2,0.2), and (1,0.4,0.4), of which (1,0.4,0.4) is the HEA polycrystalline model with the fitting parameters in the above, as shown in Fig. 5 shows

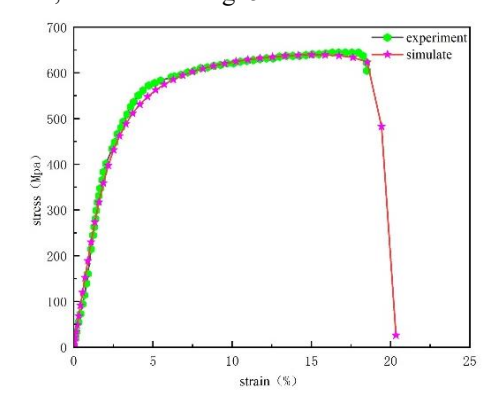


Figure.4 Comparison of polycrystalline simulation results of CoCrFeNiMn HEA with experiments

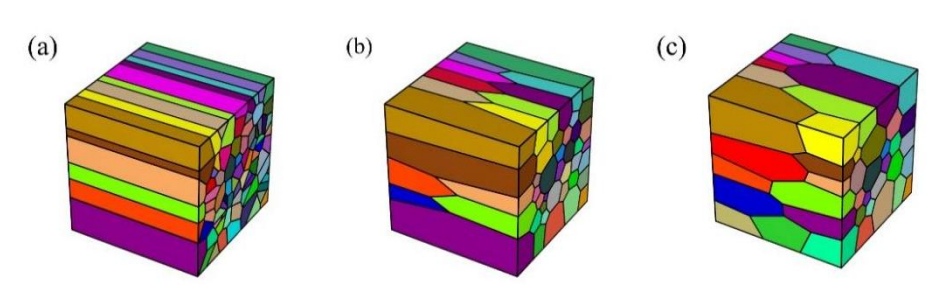


Figure.5 RVE models for different grain morphologies: (a) (1,0.1,0.1); (b) (1,0.2,0.2); (c) (1,0.4,0.4)

2.6 Polycrystalline modelling of HEA with different Texture strengths

The (1, 0.4, 0.4) polycrystalline model consisting of 80 grains is employed. Two sets of Euler angles with varying texture strengths are generated using Matlab. Subsequently, the polar plots of the initial states of the two texture configurations are created via the MTEX

software, and the plotting results are depicted in Fig. 6. Following this, Python code is utilized to assign the Euler angles of the two sets with different texture strengths to the representative volume cell and conduct the finite element simulation of crystal plasticity. The results are presented in Fig. 6.

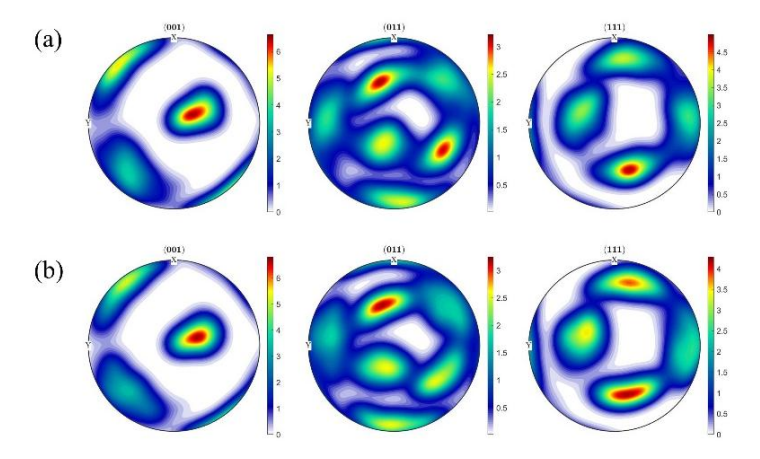


Figure.6 Polar plots of the initial state of texture for two sets of polycrystalline models of HEA: (a) texture strength 1; (b)

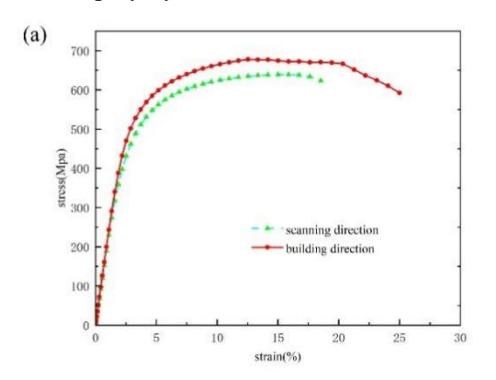
texture strength 2

3 Results and discussion

3.1 Tensile simulation of polycrystalline models of HEA with different stretching directions

Displacement loads were applied along both the scanning direction and the building direction of the CoCrFeNiMn HEA polycrystalline model to obtain stress-strain curves under different tensile orientations, as illustrated in Fig. 7(a). As shown in Fig. 7(a), no significant difference is observed between the scanning direction and the building direction in the elastic phase. However, upon fracture, the building direction exhibits superior fracture strength and toughness. These findings align with the experimental results, confirming the validity of the polycrystalline model. The simulated

polycrystalline model of the CoCrFeNiMn HEA exhibits significant anisotropy. As illustrated in Fig. 7(b), the yield strengths are 418.5 MPa (scanning direction) and 433 MPa (building direction), while the tensile strengths reach 639 MPa and 677.8 MPa, respectively. The corresponding elongations are 16.7% and 22.1%. The polycrystalline CoCrFeNiMn HEA exhibits yield strength anisotropic coefficient of 3.3%, tensile strength anisotropic coefficient of 5.7%, and elongation-at-break anisotropy of 22.4%. This difference in properties is mainly due to the 'top-down' heat transfer characteristic of SLM, which leads to the generation of columnar crystals along the building direction, resulting in better mechanical properties in the deposition direction than in the scanning direction^[24].



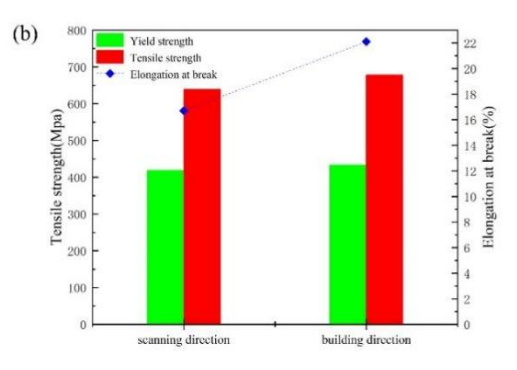


Figure.7 CoCrFeNiMn HEA polycrystalline model building direction vs. scanning direction: (a) tensile stress-strain curve; (b) comparison of mechanical properties

3.2 Tensile simulation of polycrystalline models of HEA with different grain morphologies

To investigate the influence of grain morphology on the mechanical properties of CoCrFeNiMn HEA polycrystals, finite element tensile simulations were performed on polycrystalline models with average aspect ratios of (1, 0.1, 0.1), (1, 0.2, 0.2), and (1, 0.4, 0.4). The stress-strain relationships during the simulation of polycrystalline models with different grain shapes are shown in Fig. 8(a). It is found that as the aspect ratio of the polycrystalline model gets smaller, there is no significant difference in the elastic phase of the polycrystalline model, but the tensile strength of the material increases and the plasticity is significantly enhanced. The CoCrFeNiMn HEA polycrystalline model with average aspect ratios of (1,0.1,0.1), (1,0.2,0.2), (1,0.4,0.4) and the yield strengths obtained from the

simulations are 423Mpa, 436.9Mpa and 418.5Mpa, and the tensile strengths are 605Mpa, 639Mpa, 639Mpa, respectively. The elongation was 7.7%, 10.6% and 16.7%, respectively, as shown in Fig. 8(b). Moreover, the (1,0.2,0.2) polycrystalline model does not exhibit a significant strength enhancement compared to (1,0.4,0.4), indicating that smaller aspect ratios have a diminishing influence on strength but a more pronounced effect on post-fracture elongation. This is due to the gradual equiaxialization of the grains, the random orientation of the equiaxial crystals and the uniform distribution of grain boundaries makes the dislocations in the traverse orientation of different grains by the grain boundary obstruction, the formation of dislocations plugging, to promote the effect of work hardening, and effectively improve the plasticity of the material.

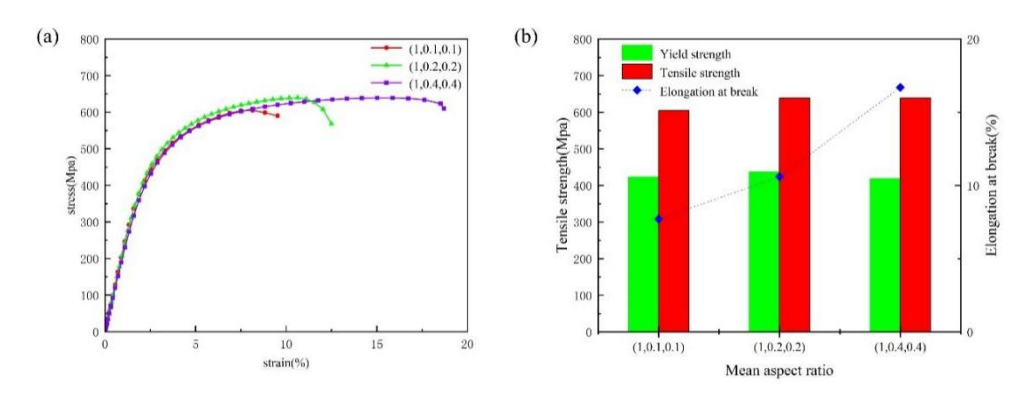


Figure.8 Polycrystalline models of three different morphologies of HEA: (a) tensile stress-strain curves; (b) comparison of mechanical properties

Load displacements were applied along the scanning and building directions of CoCrFeNiMn HEA polycrystalline models with average aspect ratios of (1, 0.2, 0.2) and (1, 0.4, 0.4), respectively. This was conducted obtain stress-strain curves for polycrystalline models with varying grain morphologies under different tensile orientations and to investigate the influence of columnar-to-equiaxed grain transition on the of SLM CoCrFeNiMn HEA. anisotropy polycrystalline model stress-strain curves show obvious anisotropy, which is in agreement with the experimental results and proves that the simulation results are reliable. The results show that the average aspect ratio (1,0.2,0.2)polycrystalline model exhibits significant anisotropy, with yield strengths of 436.9 MPa and 484.7 MPa in the

scanning direction and deposition direction, respectively, and tensile strengths of 639 MPa and 702.5 MPa, respectively, with elongations of 10.6% and 21.8%, as shown in Fig. 9(a). The anisotropy coefficient of yield strength is 10.9%, the anisotropy coefficient of tensile strength is 9%, and the anisotropy coefficient of elongation at break is 51.4% for the polycrystalline model with an average aspect ratio of (1,0.2,0.2); The anisotropy coefficients of yield strength, tensile strength, and, postbreak elongation were reduced by 7.6%, 3.3%, and 27%, respectively, for the average aspect ratio (1,0.4,0.4) polycrystalline model compared to (1,0.2,0.2)polycrystalline model, which indicates that columnarcrystalline equiaxialization effectively improves the anisotropy of CoCrFeNiMn HEA, as shown in Fig. 9(b).

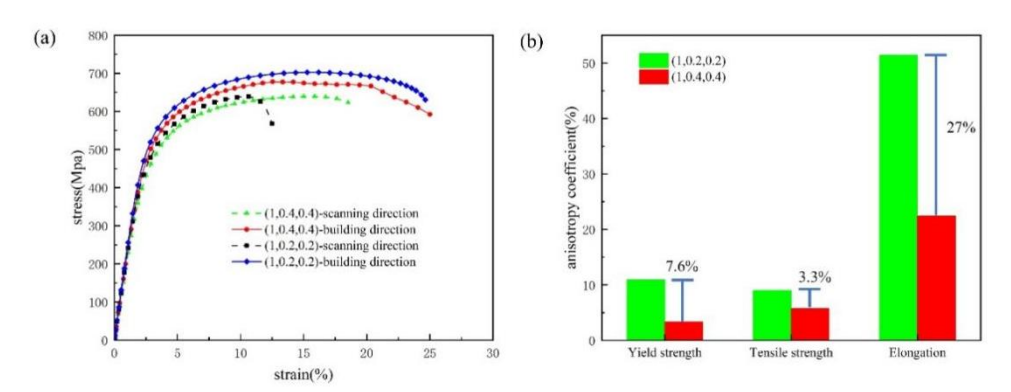


Figure.9 Polycrystalline models of three different morphologies of HEA: (a) tensile stress-strain curves; (b) comparison of mechanical properties

3.3 Tensile simulation of polycrystalline models of HEA with different Texture strengths

While keeping all other parameters of the CoCrFeNiMn HEA polycrystalline model constant, only the initial crystallographic texture was altered to investigate its influence on crack initiation and propagation during tensile fracture. Figure 10 shows the simulation results of tensile fracture for two different

Texture strengths. As can be seen from Fig. 10, the two different Texture strength polycrystalline models have different locations of crack initiation and extension, and there is a significant difference in the location of fracture, for example, the location of cracks in the polycrystalline model of Texture strength 1 does not occur in the polycrystalline model of Texture strength 2 fracture phenomenon.

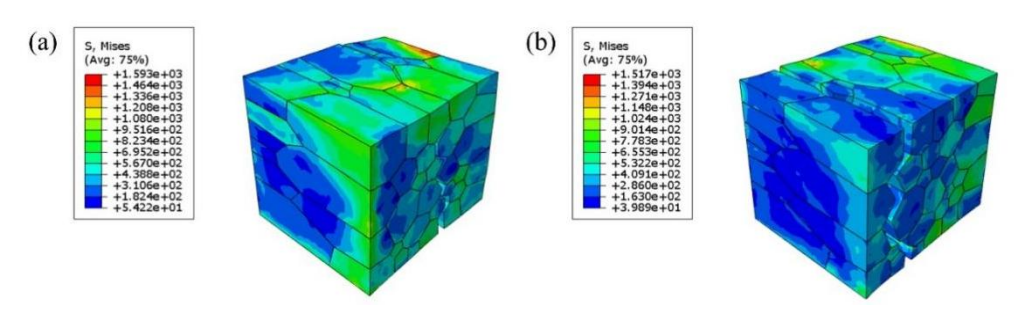


Figure.10 Simulation results of tensile fracture: (a) Texture strength-1; (b) Texture strength -2

Further analysis of SEDGs with varying texture strengths demonstrated that differences in texture strength influence the crack initiation sites and final fracture locations in polycrystalline models. Figure 11 shows the results of grain boundary damage at different stages of the two Texture strengths, the grain boundary unit is deleted to represent the fracture of the grain boundary, and the different fracture locations of the two polycrystalline models can be clearly observed in the figure. In the polycrystalline model at Texture strength-1, the cohesive element at position 1 has been deleted and the grain boundaries here have undergone fracture behaviour, but at

the same position at Texture strength-2 the grain boundaries have undergone little damage. In the polycrystalline model with Texture Strength-1, grain boundary damage is observed at Position 2; however, the damage variable D does not attain a value of 1, suggesting that fracture behavior does not occur at this boundary. In contrast, for the model with Texture Strength-2, the cohesive element at the same position is deleted, indicating that the damage variable D reaches 1 and fracture initiates. These results demonstrate that variations in texture strength influence the crack initiation site during tensile fracture in polycrystalline materials.

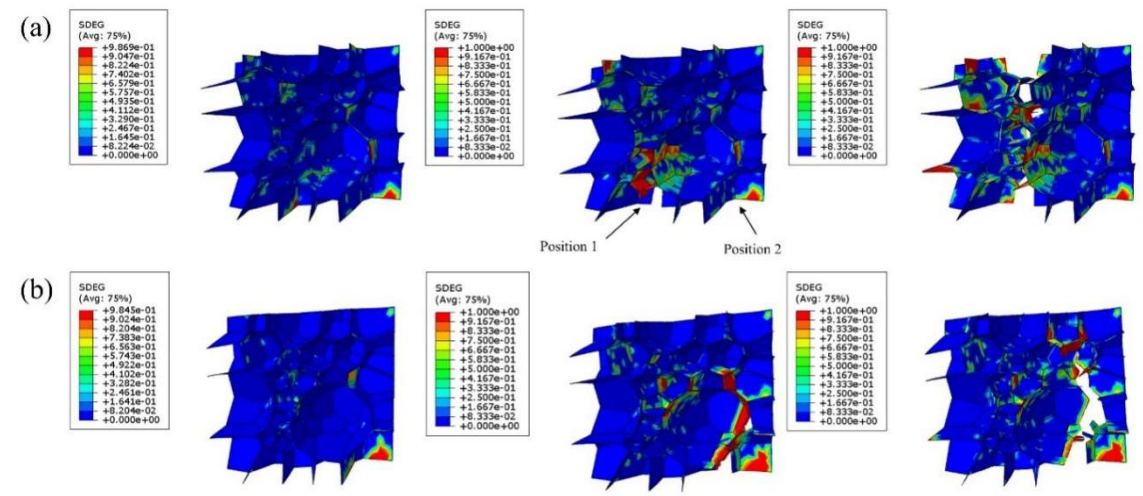


Figure.11 SEDG simulation results for different stages of grain boundary: (a) Texture strength-1; (b) Texture strength-2

Fig. 12(a) shows the stress-strain curves for tensile fracture of two different Texture polycrystalline models, and there is no significant difference between the two sets of curves in the elastic phase. The yield strength, tensile strength, and post-break elongation of Texture strength-1 are 447.6 Mpa, 688.7 Mpa, and 11.7%, respectively; and the yield strength, tensile strength, and post-break

elongation of Texture strength-2 are 418.5 Mpa, 639 Mpa, and 16.7%, respectively, as shown in Fig. 12(b). It indicates that different Texture strengths not only affect the crack initiation and extension at the grain boundaries, but also affect the macroscopic mechanical response of polycrystals.

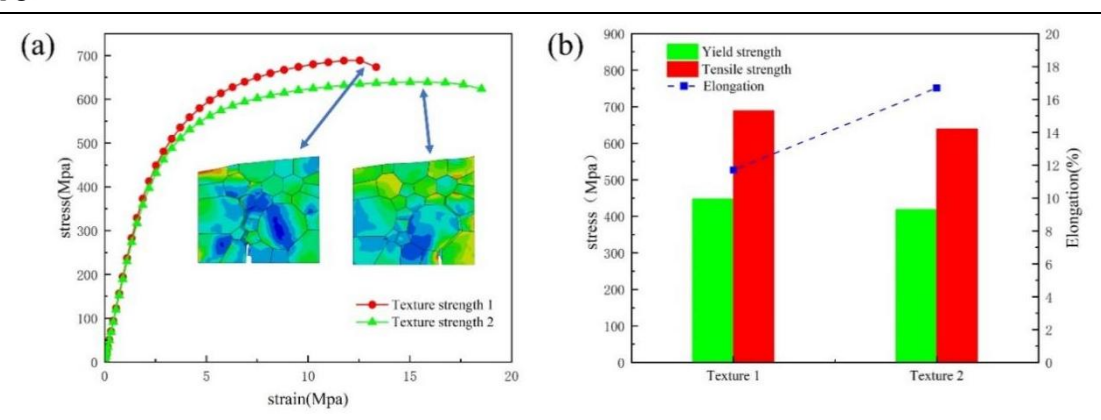


Figure.12 Different Texture polycrystalline models: (a) tensile stress-strain curves; (b) comparison of mechanical properties

4 Conclusions

In this paper, the tensile fracture behaviour of CoCrFeNiMn HEA is studied from micro-scale by means of crystal plasticity finite element theory and cohesive unit, and the main conclusions are as follows:

- (1)The stress-strain curve of CoCrFeNiMn HEA at tensile fracture is effectively simulated based on the crystal plasticity intrinsic model and cohesive intrinsic model, and the simulated post-break elongation is 16.7%, and the tensile strength is 639 MPa.
- (2)The CoCrFeNiMn HEA under different tensile directions show obvious anisotropy, with an anisotropy coefficient of yield strength of 3.3%, tensile strength of 5.7%, and post-break elongation of 22.4% in scanning direction and building direction.
- (3)The polycrystalline elongation of CoCrFeNiMn HEA with different grain morphologies increases from 7.7% to 16.7% and the anisotropy coefficients of yield strength, tensile strength, and elongation decrease by 7.6%, 3.3%, and 27%, respectively, when the average aspect ratio decreases, i.e., when columnar crystals are gradually equiaxialized.
- (4)Different Texture strengths significantly affect the crack initiation and extension of CoCrFeNiMn HEA, as well as the macroscopic mechanical response of the polycrystalline model.

Acknowledgments

Authors acknowledge the funding supported by National Natural Science Foundation of China (Grant No. 52175359)

References

- [1] Yeh J.W., S.K. Chen, S.J. Lin, et al. Nanostructured high-entropy alloys with multiple principal elements: novel alloy design concepts and outcomes. Advanced engineering materials, 2004, 6(5): 299-303.
- [2] Wang P., P. Huang, F.L. Ng, et al. Additively manufactured

- CoCrFeNiMn high-entropy alloy via pre-alloyed powder. Materials and Design, 2019, 168: 107576.
- [3] Vaidya M., K. Pradeep, B. Murty, et al. Bulk tracer diffusion in CoCrFeNi and CoCrFeMnNi high entropy alloys. Acta Materialia, 2018, 146: 211-224.
- [4] Butler T.M., M.L. Weaver. Oxidation behavior of arc melted AlCoCrFeNi multi-component high-entropy alloys. Journal of Alloys Compounds, 2016, 674: 229-244.
- [5] Stepanov N., M. Tikhonovsky, N. Yurchenko, et al. Effect of cryo-deformation on structure and properties of CoCrFeNiMn high-entropy alloy. Intermetallics, 2015, 59: 8-17
- [6] Laplanche G., A. Kostka, O. Horst, et al. Microstructure evolution and critical stress for twinning in the CrMnFeCoNi high-entropy alloy. Acta Materialia, 2016, 118: 152-163.
- [7] Zhou Z., C. Ji, D. Hou, et al. Study on Mechanical Properties of Nanopores in CoCrFeMnNi High-Entropy Alloy Used as Drug-Eluting Stent. Materials, 2024, 17(13): 3314.
- [8] Brif Y., M. Thomas, I. Todd. The use of high-entropy alloys in additive manufacturing. Scripta Materialia, 2015, 99: 93-96.
- [9] Gu X.H., T. Lu, T. Zhang, et al. Anisotropy of microstructures and mechanical properties in FeCoNiCr0. 5 high-entropy alloy prepared via selective laser melting. Rare Metals, 2022, 41(6): 2047-2054.
- [10] Kim Y.K., J. Choe, K.A. Lee. Selective laser melted equiatomic CoCrFeMnNi high-entropy alloy: Microstructure, anisotropic mechanical response, and multiple strengthening mechanism. Journal of Alloys Compounds, 2019, 805: 680-691.
- [11] Ng C., H, M. Bermingham, J, M. Dargusch, S Controlling grain size, morphology and texture in additively manufactured β-titanium alloy with super transus hot isostatic pressing. Additive Manufacturing, 2022, 59: 103176.
- [12] Duan W, Dang L X, Zhou J X, et al. Advancements in hot isostatic pressing as post-processing technique for additively manufactured titanium alloy components. Development and Application of Materials, 2024, 39(01): 105-116.
- [13] Dolzhenko A., M. Tikhonova, R. Kaibyshev, et al.

- Microstructures and mechanical properties of steels and alloys subjected to large-strain cold-to-warm deformation. Metals, 2022, 12(3): 454.
- [14] Cai W., C. Sun, C. Wang, et al. Modelling of the intergranular fracture of TWIP steels working at high temperature by using CZM-CPFE method. International Journal of Plasticity, 2022, 156: 103366.
- [15] Yin L.W., O. Umezawa. Crystal plasticity analysis of temperature-sensitive dwell fatigue in Ti-6Al-4V titanium alloy for an aero-engine fan disc. International Journal of Fatigue, 2022, 156: 106688.
- [16] Wang S Y , Song S J, Lu X C, et al. Tensile Fracture Behavior of the CrMnFeCoNi High Entropy Alloy: A Crystal Plasticity Finite Element Simulation. Journal Of Mechanical Engineering, 2021, 57(22): 43-51.(in chinese)
- [17] Dang L X, LI Y Y,Zhang T, et al. Microfracture Evolution Simulation of Titanium Ti-6Al-4V Duplex Layer Structure. Special Casting & Nonferrous Alloys, 2024, 1-8. (in chinese)
- [18] Wang F C. Optimization of Forming Process and Characterization of CoCrFeNiMn High Entropy Alloy Fabricated by Selective Laser Melting, Master's thesis:Huazhong University of Science & Technology,

- Wuhan:2019. (in chinese)
- [19] Peirce D., R. Asaro, A. Needleman. An analysis of nonuniform and localized deformation in ductile single crystals. Acta Metallurgica Sinica, 1982, 30(6): 1087-1119.
- [20] Manual A. ABAQUS 6.14 Analysis User's Manual. Online Documentation Help: Dassault Systemes, 2014.
- [21] Li W.s., Y.Y. Huang, Z.H. Xie, et al. Mechanical property and cellular structure of an additive manufactured FeCoNiCrMo0. 2 high-entropy alloy at high-velocity deformation. Journal of Materials Science Technology, 2023, 139: 156-166.
- [22] Quey R., P.R. Dawson, F. Barbe. Large-scale 3D random polycrystals for the finite element method: Generation, meshing and remeshing. Computer Methods in Applied Mechanics Engineering, 2011, 200(17-20): 1729-1745.
- [23] Du Plessis A., E. Macdonald. Hot isostatic pressing in metal additive manufacturing: X-ray tomography reveals details of pore closure. Additive Manufacturing, 2020, 34: 101191.
- [24] Xiong Y., F. Zhang, T. Dai, et al. Crystal growth mechanism and mechanical properties of Ti-6Al-4 V alloy during selective laser melting. Materials Characterization, 2022, 194: 112455.